ADVANCED ELECTRONIC MATERIALS Open Access
www.advelectronicmat.de

Electrochemical Doping for Absorption and Conductivity Tuning of P(NDI2OD-T2) Films

*David Neusser, Xiuming Sun, Sushri Soumya Jena, Wen Liang Tan, Lars Thomsen, Christopher R. McNeill, Sarbani Ghosh, Igor Zozoulenko, and Sabine Ludwigs**

Electrochemical doping of thin films of poly{[N,N′-bis(2-octyldodecyl)-naphthalene-1,4,5,8-bis(dicarboximide)-2,6-diyl]-alt-5,5′-(2,2′-bithiophene)} (P(NDI2OD-T2)) is shown as straightforward method to achieve different degrees of doping both during in situ electrochemical experiments as well as in the solid state. Results obtained from cyclic voltammetry and absorption spectroscopy upon reduction can be explained by the presence of the neutral state as well as polaron and bipolaron species, including neutral/polaron and polaron/bipolaron mixed valence states. The UV-vis-NIR spectra are analyzed and explained based on the calculated electronic structure and the corresponding transitions between different states, this includes features such as numbers and positions of the peaks and their evolution during reduction. Most intruingly, doped films are stable after transfer in the solid state, as evidenced by absorption spectroscopy. Conductivity measurements of films with different degrees of doping show a bell-shaped conductivity profile, which underlines the classification of P(NDI2OD-T2) as a conjugated redox polymer with mixed valence transport. Maximum conductivities of up to 2 × 10^{-4} S cm^{-1} are obtained at intermediate doping levels under the coexistence of neutral state and polarons. Conductivity measurements of blade-coated films point to anisotropic charge transport with the highest charge transport along the blade /polymer chain direction and an anisotropic conductivity ratio of 4.1.

1. Introduction

A fundamental understanding of the doping process is key to success in optimizing conducting polymer films for applications in organic electronics and electrochemical devices.[1,2] Accessibility of different degrees of doping is required for the fine-tuning of the conductivity.[3,4] Whereas many groups have shed light on doping of p-type polymers with the work-horses poly(3-hexylthiophene) (P3HT) and poly(ethylenedioxythiophene):poly(styrenesulfonate) (PEDOT:PSS), research in n-type materials and their doping and conductivity behavior is still lagging behind.[5–8] In the case of n-type semiconductors, the ladder-type polymer poly(benzimidazobenzophenanthroline) (BBL) is probably the current n-type champion, with conductivities of 8 S cm^{-1} and excellent thermal, ambient, and solvent stability.[9,10] However, also the class of n-type polymers based on backbones with NDI (naphthalenediimide) with the most prominent representative P(NDI2OD-T2) (N2200) still gets a lot of attention, especially in the context of chemical modification for organic electrochemical transistors.[11–17]

Upon reduction, negative charges are strongly localized on the NDI units, establishing a model where P(NDI2OD-T2) can be described as a sequence of isolated redox units,[18–21] underlining the classification as a conjugated redox polymer. In the case of polythiophene model systems, charges are delocalized over multiple repeating units,[22,23] being one reason for the different conductivity mechanism and behavior thoroughly discussed in the literature.[24,25]

D. Neusser, X. Sun, S. Ludwigs
IPOC – Functional Polymers
Institute of Polymer Chemistry (IPOC)
University of Stuttgart
Pfaffenwaldring 55, 70569 Stuttgart, Germany
E-mail: sabine.ludwigs@ipoc.uni-stuttgart.de

The ORCID identification number(s) for the author(s) of this article can be found under https://doi.org/10.1002/aelm.202400956

DOI: 10.1002/aelm.202400956

S. S. Jena, S. Ghosh
Department of Chemical Engineering
Birla Institute of Technology and Science (BITS)
Pilani Campus, Vidya Vihar, Pilani, Rajasthan 333031, India

W. L. Tan, C. R. McNeill
Department of Materials Science and Engineering
Monash University
Wellington Road, Clayton, Victoria 3800, Australia

W. L. Tan, L. Thomsen
Australian Synchrotron, ANSTO
800 Blackburn Road, Clayton, Victoria 3168, Australia

I. Zozoulenko
Laboratory of Organic Electronics
Linköping University
Norrköping 60174, Sweden

Besides the electronic properties, P(NDI2OD-T2) is known for its ability to show strong inter- and intrachain aggregation.[26] The aggregation behavior has been both studied in the solution as well as the solid state.[27–33] Special film coating methods like blade coating rely on pre-aggregation in solution and the tendency to show liquid crystal-like behavior.[34] We have shown in the past that blade coating leads to fiber-like morphologies in the film with the blading direction corresponding to the chain direction. This anisotropy has an influence not only on the optical properties but also on charge transport mobility and conductivity as presented in the literature.[34–37] A recent publication by Bredas and coworkers further gives insights into polymorphism as a function of deposition and post-annealing treatment.[38]

Typically, P(NDI2OD-T2) is doped using a chemical doping approach based on dopants like 4-(2,3-dihydro-1,3-dimethyl-1H-benzimidazol-2-yl)-N,N-dimethylbenzeneamine (N-DMBI) or tetrakis(dimethylamino)ethylene (TDAE).[20,39,40] In the case of TDAE the dopant has a strong tendency to donate electrons to the LUMO of P(NDI2OD-T2).[41] Drawbacks of this chemical doping approach are that it typically suffers from low doping efficiencies due to aggregation of dopant molecules.[1,6] Additionally, the formation of locally bound charge transfer complexes is reported to disturb integer charge transfer which limits the overall amount of accessible mobile charge carriers.[42,43]

Theoretical insights into these systems—particularly for naphthalenediimide (NDI)-based polymers—remain limited and underdeveloped compared to their p-doped counterparts. Only recently, theoretical studies have for example uncovered how dopants stabilize the NDI polymer structure.[44] Molecular dynamics (MD) simulations probed the interactions between dopants and polymer backbones and alkyl chains, while density functional theory (DFT) calculations provided details on molecular geometry, electronic density distribution, and energy levels of frontier orbitals, as well as FTIR spectra.[45–47] Other studies on closely related NDI-based n-type copolymers contribute to an advanced understanding of these complex materials.[48–50]

Interestingly, theoretical insights into how the optical absorption spectra of P(NDI2OD-T2) evolve with varying reduction levels are nearly nonexistent. NDI-based polymers exhibit a far more complex optical absorption pattern than well-studied p-doped thiophene-based conducting polymers.[24] Specifically, while thiophene-based polymers display only one or two absorption peaks depending on the doping level, P(NDI2OD-T2) can present anywhere from two to four peaks. Furthermore, the optical absorption of undoped (neutral) material closely resembles that of its fully doped counterpart—a contrast to p-doped polymers, where the neutral and fully doped states have distinctly different absorption bands. As of now, there is no theoretical explanation that addresses these puzzling and intriguing features.

In this study, we report a comprehensive in situ spectroelectrochemical study on the doping behavior of P(NDI2OD-T2) films which is supported by DFT calculations and allows us to analyze the complex evolution of the spectra and charged states of the polymer (i.e., neutral to polaronic to bipolaronic) based on the calculated electronic structure as the reduction level increases.

Following an approach recently established for P3HT[51,52] we further demonstrate that the differently doped states obtained by electrochemical doping can be transferred into the solid state. The conductivity of the doped films as a function of the doping potential is monitored using 4-line probe measurements. In good agreement with the prediction of the mixed valence conductivity model, the conductivity follows a bell-shaped behavior and gives a highest conductivity of up to 2×10^{-4} S cm^{-1} which corresponds to the coexistence of neutral state and polarons. Electrochemical doping and conductivity measurements on aligned films prepared by blade coating gives maximum conductivities of $\sigma_{\parallel} = 1.6 \pm 0.5 \times 10^{-4}$ S cm^{-1} in the direction of chain alignment, which is by a factor of 4.1 higher compared to the conductivities measured perpendicular to the alignment direction. The role of counterion incorporation and change of morphology are discussed with the help of ex situ grazing-incidence wide-angle X-ray scattering (GIWAXS).

Figure 1 summarizes our electrochemical doping approach and chemical structures of the charged species of P(NDI2OD-T2).

2. Results and Discussion

2.1. In Situ Spectroelectrochemistry and Theoretical Modeling of the Absorption Spectra

In situ spectroelectrochemistry experiments allow us to study the occurrence of charged species of P(NDI2OD-T2) during electrochemical reduction by UV-vis-NIR spectroscopy. We have shown in earlier publications that P(NDI2OD-T2) allows for a two-step reduction with charges mainly localized on the NDI units: first to radical anions, which corresponds to one charge per repeating unit with 50% reduction (C_{red} = 50%), and then dianions, meaning two charges per repeating unit with 100% reduction (C_{red} = 100%).[24,37,41] This two-step process can be clearly seen in the second cycle of the cyclic voltammogram (see **Figure 2a**) where two separated sets of redox waves are visible:[24] set I refers to the first reduction and set II refers to the second reduction. The appearance of multiple redox waves for the first and second reduction is very characteristic for P(NDI2OD-T2), and found for different molecular weights, regioregularities, and thermal treatment, and the redox potentials are all very similar for different P(NDI2OD-T2) samples.[24,37,41] Please note that the reduction waves are clearly separated from each other by potential regions which show zero current. In the CV these regions are colored in blue for the fully neutral, green for the first reduced and red for the second reduced state. We will call the radical anion polaron state and the dianion bipolaron state throughout the manuscript.

The half-wave potential for the first electron transfer is around $E_{1/2} = -1.0$ V (all potentials are referenced versus Fc/Fc$^+$). The onset reduction potential is determined at $E_{onset} = -0.98$ V using the tangent method, which results in a LUMO of $E_{LUMO} = -3.82$ eV.

Our assignment to the redox species is supported by in situ absorption spectroscopy coupled to the CV measurements. The characteristic spectral signatures of the charged species allow for the assignment of the potential dependent redox species (see Figure 2a–c). The neutral state (blue spectrum) has a high energy peak at 385 nm and a second peak at higher wavelengths at 673 nm marked as N1 and N2. When decreasing the electrochemical potential, a gradual change of the blue spectrum into the green spectrum is visible. The characteristic spectrum of the first reduced state (polaron) shows absorption peaks at 368, 492,

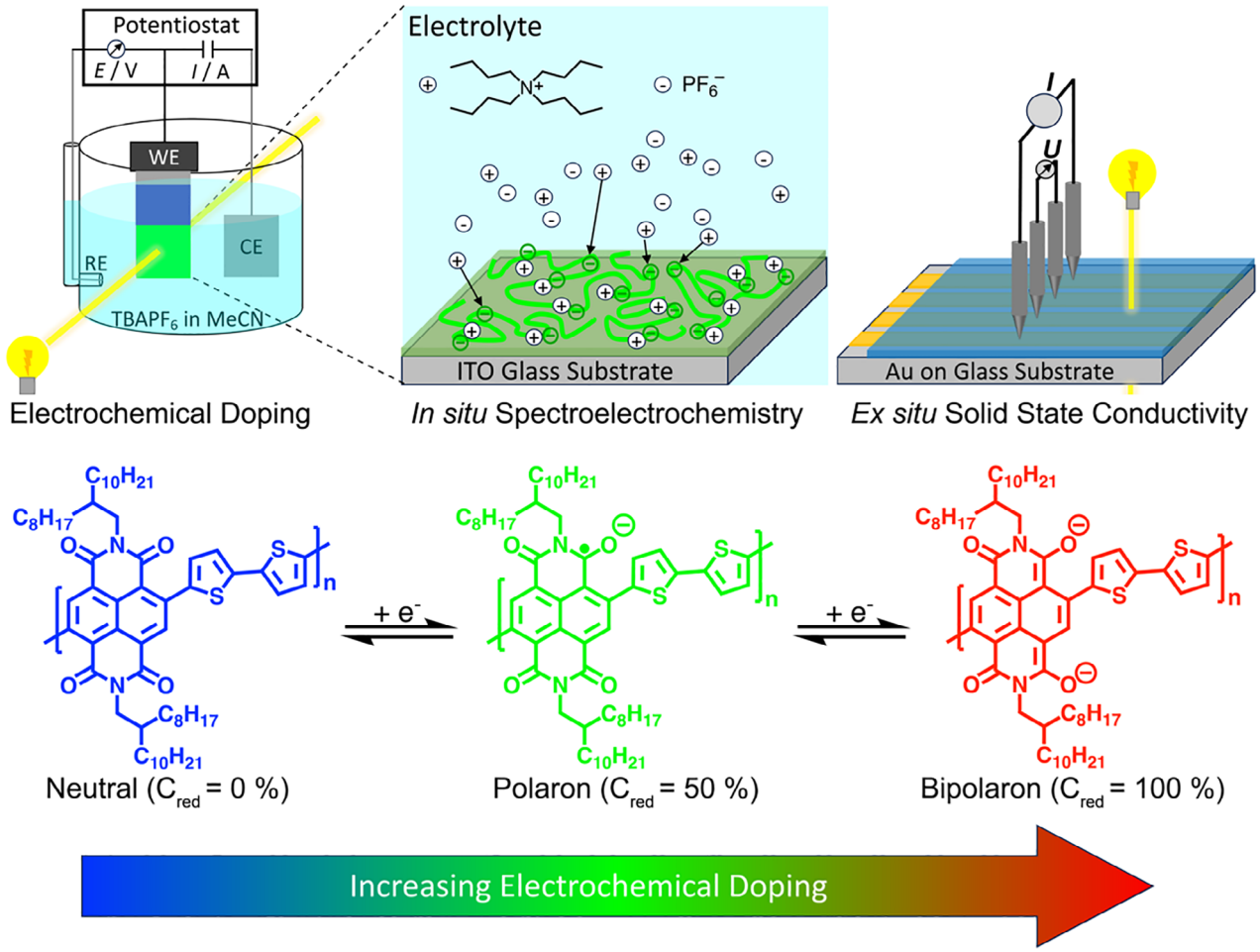

Figure 1. Schematic representation of the electrochemical doping inside a three-electrode setup using 0.1 M $TBAPF_6$ in acetonitrile as electrolyte by in situ spectroelectrochemistry. Doped films are taken out of the setup under inert conditions and ex situ follow up experiments are conducted with conductivity measurements and UV-vis-NIR spectroscopy. Chemical structures are shown for different degrees of doping: neutral, polaron (radical anion) and bipolaron (dianion).

700, and 800 nm marked as P1 through P4. Especially the peak at 492 nm is distinct and correlates with the presence of maximum polaron species from an electrochemical potential of -1.24 to -1.29 V. Further decreasing the potential below this value induces the transition into the second reduced state (bipolaron). This transition is accompanied by another significant change in the absorption spectrum (red spectrum) with two new signals rising at 392 and 713 nm marked as B1 and B3. Note that the spectrum exhibits a shoulder between B1 and B3 at $\lambda \approx 550$ nm, which we mark as B2.

Remarkably, by comparing the optical absorption behavior in the first cycle with the second cycle, we observed that the broad low energy absorption band of the neutral spectrum was shifted from 700 to 673 nm accompanied with a decrease in the absorbance (see Figure S2, Supporting Information). We also observed that both reduction peaks in the signal set I appear at more positive potentials in the forward scan of the second cycle than the first cycle (see Figure S1, Supporting Information). This behavior is due to a first-cycle effect which can be explained by a reduction of the aggregate content in the film due to counterion and solvent diffusion during the first charging.[24] The first cycle effect was shown to strongly depend on film morphology and degree of crystallization.[24] It also points to strong correlations between morphology and electrochemical doping.[53]

Let us now analyze the experimental findings based on the theoretical predictions. For many years, the theoretical understanding of the electronic structure and optical properties of conducting polymers relied on "traditional" semiempirical theories, which were introduced over forty years ago, long before the DFT approach became the standard in computational materials science and chemistry.[54] In the case of p-doped polymers, there is now a growing consensus that these "traditional" methods should be replaced by modern DFT-based models.[55–59] These models provide distinct predictions for observable properties, such as the evolution of absorption spectra, spin structure, and electronic structure, which match experimental spectra and differ qualitatively from the predictions of the "traditional" approaches.[59,60] Much less theoretical work has so far been done on absorption spectra of n-doped polymers. These works include investigation of the optical absorption at

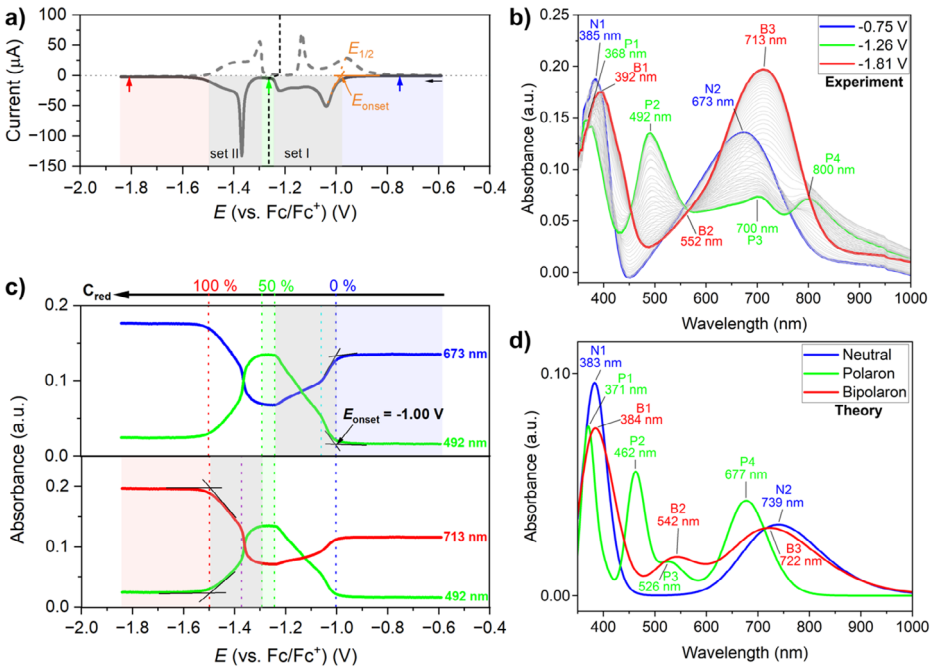

Figure 2. a–c) In situ spectroelectrochemistry measurements of a spin-coated film of P(NDI2OD-T2) on an ITO glass substrate upon reduction, scan rate 20 mV s^{-1} in 0.1 M $TBAPF_6$/acetonitrile electrolyte. (a) Second cycle of reduction. (b) UV–vis absorption spectra recorded in situ during the forward scan. The characteristic spectra for the neutral (N), polaron (P), and bipolaron (B) states of P(NDI2OD-T2) are indicated by blue (N1, N2), green (P1, P2, P3, P4), and red (B1, B2, B3) spectra. (c) Spectral evolutions of characteristic peaks at 673 nm (N2), at 492 nm (P2), and at 713 nm (B3) are plotted as function of potential during the forward scan. The blue, green, and red shading indicate the potential ranges of the fully neutral, fully polaron, and fully bipolaron states, respectively. The gray shading refers to the potential ranges for the transition from the neutral to polaron (set I) and from polaron to bipolaron states (set II), i.e., potential ranges for mixed charged species. d) TD-DFT calculated UV–vis absorption spectra of neutral and charged states of an NDI-T2 dimer are shown.

different reduction levels for the archetypical n-doped conducting polymer, double-stranded benzimidazo-benzophenanthroline ladder (BBL), K-doped polyfluorene films, and p-type/n-type polymer blends.[61–63]

In the present work, to gain further insight into the optical properties of the neutral state, the first reduced state (polaronic state) and the second reduced state (bipolaronic state) of P(NDI2OD-T2), we compared experimentally measured spectra with TD-DFT calculated absorption spectra performed at B3LYP /6-31+G(d) level of theory (see Figure 2d) and analyzed them on the basis of DFT-calculated electronic structures performed at the same level of theory.[64] For the simulation, we used the dimer $(NDI\text{-}T2)_2$ consisting of naphthalene diimide (NDI) units (with a methyl side group) alternating with two bithiophene groups (T2) as the model system for the copolymers.

In Figure 2d, the calculated absorption spectra show the same peak structure and number of peaks as the experimental results: peaks N1 and N2 for the neutral system at 0% doping level; peaks P1, P2, P3, and P4 for the polaron state at 50% doping level, and peaks B1, B2, and B3 for the bipolaron state at 100% doping level. The peak positions in the experimental and calculated spectra show good agreement, leading us to conclude that TD-DFT calculations provide a quantitative match with the observed spectra. It is noteworthy that we also performed the same TD-DFT calculations with the long-range corrected hybrid functional ωB97XD. In this case we found only qualitative agreement of the calculated and experimental spectra where the peak positions do not exactly match each other (see Figures S3 and S5, Supporting Information). It is interesting to note that for p-doped polymers, the hybrid functional B3LYP also provides a superior description of the experimental spectra compared to the ωB97XD functional.[59]

Due to the quantitative agreement between the measured and calculated spectra, we can now explain the origin and evolution of peaks in the absorption spectra through the changes in the calculated electronic structure and the corresponding optical transitions. **Figure 3** shows the calculated electronic structure of $(NDI\text{-}T2)_2$ as the reduction level changes from C_{red} = 0% to 100%. The occupied states within the valence band and the unoccupied states in the conduction band are depicted via blue and red lines, respectively; the occupied polaron and bipolaron states are depicted by dashed blue lines. For *n*-doped polymers the polaron is a singly occupied electron state, corresponding to the case when the spin degeneracy is lifted, whereas the bipolaron is spin-degenerated state with zero spin occupied by two electrons.[59] The up (↑) and down arrows (↓) signify the spin-up and spin-down orbitals, respectively (also often called α and β orbitals in quantum-chemical calculations).

Neutral state (C_{red} = 0%)

The calculated electronic structure of neutral $(NDI\text{-}T2)_2$ shows the valence and conduction states separated by the gap, where the electronic distribution of the highest occupied molecular

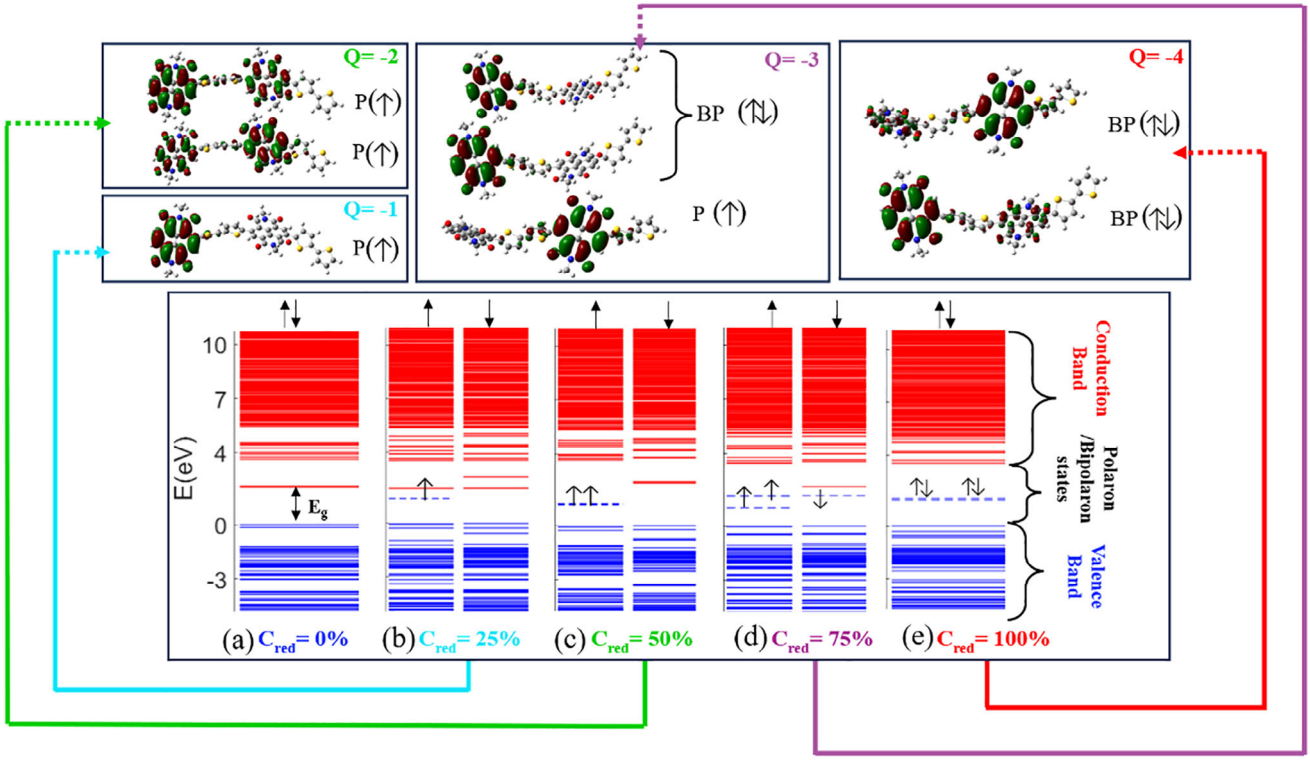

Figure 3. Energy band diagram of NDI-T2 dimer for different reduction levels a) C_{red} = 0%, b) C_{red} = 25%, c) C_{red} = 50%, and d) C_{red} = 75%, and e) C_{red} = 100%. The occupied states within the valence band and the unoccupied states in the conduction band are depicted via blue and red lines, respectively; the occupied polaron and bipolaron states within the energy band diagram are depicted by dashed blue lines. The corresponding electron distribution of polaron and bipolaron states are shown in the inset figures.

orbitals, HOMO and HOMO-1 are localized on the bithiophene (T2) moieties (donor unit), whereas HOMO-2 is localized on both T2 (donor unit) and the NDI (acceptor unit) moieties, see Figure S4a (Supporting Information). For the valence band, the character of the states is exactly the opposite, LUMO and LUMO+1 are localized on the acceptor unit, whereas LUMO+2 is localized at the donor unit. Because the repeating unit of NDI-T2 consists of two different moieties, its electronic structure shows miniband formation, with the groups of different states (localized at different moieties) in the conduction and valence bands being separated by minigaps. Note that the miniband structure persists even at higher oxidation levels, as can be seen in Figure 3b–d.

The formation of the miniband structure results in two distinct peaks in the absorption spectrum, N1 and N2. The origin of these peaks is outlined in Figure S3a (Supporting Information), which details the transitions contributing to each peak. The lowest energy peak N2 is due to the HOMO→LUMO transition (i.e., transition between the donor and acceptor moieties), whereas peak N1 is due to the transition from the HOMO to the higher-energy miniband in the conduction band (i.e., transition within donor moieties). It is noteworthy that miniband formation, resulting in the presence of two peaks in the absorption spectra, also occurs in another important *n*-type polymer, benzimidazo-benzophenanthroline ladder (BBL), which features a double-stranded ladder structure, as well as in the NDI-based polymer with conjugated and non-conjugated donor units.[48,61]

Polaron States

C_{red} = 25%: The first polaronic state corresponds to one electron in the NDI-T2 dimer with Q = -1, i.e., one electron per every second monomer unit. Addition of an electron results in lifting the spin degeneracy between the spin-up and spin-down states of the corresponding neutral system, see Figure 3b. A polaron is formed in the spin-up state (α-electron) and localized only on one of the NDI units (Figure 3b), whereas the other NDI unit is in the neutral state. Because of this, we will refer to this state as the coexistence of the neutral state and polaron.

C_{red} = 50%: The fully polaronic state corresponds to two electrons in the NDI-T2 dimer with Q = -2, i.e., one electron per each monomer unit. In this case, the spin degeneracy is also lifted similar to C_{red} = 25%, leading to the triplet state. Note that calculations show that this state has an energy that is lower than the energy of a spin-degenerate singlet state as shown in Figure S7 (Supporting Information), which agrees well with Hund's rule. The added electrons occupy polaron states of the same spin, that are spatially localized on two different NDI units, i.e., 1st NDI unit (NDI-1) and 2nd NDI unit (NDI-2), see inset of Figure 3c. We will refer to this state as the polaronic state, as each monomer accommodates one polaron.

The polaron state shows a total of four peaks (P1, P2, P3, and P4) both in TD-DFT calculated and experimentally measured spectra, see Figure 2b,d. The origin of these peaks is detailed in Figure S3c (Supporting Information). The lowest energy peak

(P4) corresponds to the electronic transition from the highest occupied polaronic state to the lowest unoccupied state in the spin-up state (this transition is defined as T_P in Figure S3c, Supporting Information). Peak P1 corresponds to the transitions from the valence to a miniband in the conduction bands (transitions are defined as T_V). The peaks P2 and P3 are due to transitions between the valence and conduction bands with some admixture of the transition from the occupied polaronic states to a miniband in the conduction band (transitions are defined as T_{P+V}).

C_{red} = 75%: The electronic structure of $(NDI\text{-}T2)_2$ for the case of C_{red} = 75%, i.e., three electrons in the dimer (Q = -3), shows the formation of one spin-up polaron (α-electrons), and one spinless bipolaron. This means that both polaron and bipolaron are present in the same chain, Figure 3d. We therefore will refer to this case as the mixed polaron-bipolaron state. The bipolaron (a degenerate pair of two spatially indistinguishable polarons having opposite spins) is localized on the NDI-1 moiety, and the polaron with spin-up is localized on the NDI-2 moiety. It is noteworthy that the coexistence of polarons and bipolarons on the same chain was also predicted for the n-type conducting polymer BBL.[59] The absorption spectra of $(NDI\text{-}T2)_2$ for the case C_{red} = 75% show three distinct peaks (Figure S3d, Supporting Information). The lowest energy peak shows the electronic transition from the highest occupied bipolaronic energy levels of both spin-up and spin-down states to the respective lowest unoccupied states in the conduction band (T_P transition) (Figure S3d, Supporting Information). The second lowest energy peak originates from the transition from one of the spin states of the bipolaron to the LUMO (T_P transition). The highest energy peak originates from the transition from valence band to the LUMO in spin-down state with some admixture of the transition from the occupied polaronic states to the LUMO in spin-up state (T_{P+V} transition) (Figure S3d, Supporting Information).

Bipolaron State (C_{red} = 100%)

The bipolaron state corresponds to four electrons in $(NDI\text{-}T2)_2$, i.e., two electrons per monomer unit (Q = -4). With an even number of electrons per repeating unit, the spin degeneracy of the electronic structure is restored, resulting in the formation of two distinct, but energetically close bipolaron states. Each of these states accommodates two electrons, resulting in one bipolaron per NDI moiety, Figure 3e. We therefore will refer to this case as the bipolaronic state. The bipolaron state exhibits two pronounced peaks, B1 and B3, and a broad shoulder peak B2, between B1 and B3, Figures 3b and 2d. These peaks result from transitions T_v, T_p, and T_p for peaks B1, B2, and B3 respectively (Figure S3e, Supporting Information).

It is interesting to note that the absorption spectrum of a neutral $(NDI\text{-}T2)_2$ (C_{red} = 0%) is very similar to the one of a reduced $(NDI\text{-}T2)_2$ in the bipolaronic state (C_{red} = 100%). Indeed, both of them show two pronounced peaks centered at close wavelengths: N1 and N2 for neutral $(NDI\text{-}T2)_2$, and B1 and B3 (and a weak shoulder B_2) for the bipolaronic $(NDI\text{-}T2)_2$, Figure 2b,d. At the same time, they are quite different from the spectrum of $(NDI\text{-}T2)_2$ in the polaronic state (C_{red} = 50%) that shows four pronounced peaks (P1, P2, P3, and P4). We argue that this is not a coincidence but reflects features and evolution of the electronic and spin structure of this polymer when the reduction level increases. Indeed, the electronic structure of both neutral and bipolaron $(NDI\text{-}T2)_2$ is spin-degenerate and shows very similar features, c.f. Figure 3a,e. In particular, for both cases the HOMO level represents a molecular orbital separated from the rest of the states in the valence band. Because of the similarity in the energy level structure, the electronic transitions contributing to corresponding absorption peaks are similar, c.f. Figure S3a,e (Supporting Information). In contrast to the neutral and bipolaronic states of $(NDI\text{-}T2)_2$, the spin degeneracy of the electronic structure of $(NDI\text{-}T2)_2$ in the polaronic state (C_{red} = 50%) is lifted. As mentioned above, this state is a triplet, where two polaronic states are formed for spin-up electrons, and no polaron states exist for spin-down electrons, see Figure 3c. As a result, the electronic structures of spin-up and spin-down states are rather different, which opens up the possibility for more different transitions as compared to the spin-degenerate case. In particular, transitions between spin-up states contribute to three peaks (P2, P3, and P4), and between spin-down states to three peaks (P1, P2, P3), (Figure S3c, Supporting Information). The same applies also for the cases of the coexistence of the neutral state and the polaron (C_{red} = 25%) and the mixed polaron-bipolaron state (C_{red} = 75%).

Finally, it is interesting to note that the absorption spectra of thiophene-based polymers, such as PEDOT, exhibit fewer peaks in the absorption spectra (one peak in the neutral state, two peaks at intermediate doping level, and one peak at higher doping levels).[58,65] This occurs because these polymers are composed of repeating units of the same type, and, therefore, miniband structure in the electronic spectra does not form. At the same time, the miniband structure in P(NDI2OD-T2) is retained at all doping levels. This leads to a larger number of possible transitions (i.e., transitions to/from different minibands), and therefore, to a larger number of peaks in the absorption spectra in comparison to thiophene-based polymers that are composed of the same repeating units.

Having understood the evolution of the electronic structure in $(NDI\text{-}T2)_2$ with the change of reduction level, we can provide a better interpretation of the electrochemical doping process of P(NDI2OD-T2), by relating observed features of the CV to the character of the charged states in the polymer. Let us focus on the evolution of the representative peaks in the spectra that can be clearly attributed to different reduction states, peak N2 of the neutral state at 673 nm, peak P2 of the polaron at 492 nm, and the bipolaron peak B3 at 713 nm, see Figure 2a,c.

Reduction set I: Upon decreasing the potential the polymer stays neutral at a doping level of 0% in the interval from -0.6 up to -1.0 V (marked by a blue shading in Figure 2a,c). The CV shows that the current is zero in this potential range which means that there is no charge. The absorbance at 673 nm starts to decrease and the absorbance at 492 nm simultaneously increases around the onset reduction potential of -1.0 V (vertical dark blue line), they reach their respective minimum and maximum ≈-1.26 V which is just after the appearance of the second reduction peak in the potential window of set I. Please note that the slope of both peak trends seems to change at ≈-1.06 V, which is indicated by a vertical light blue line in Figure 2c. In accordance with the calculations one might assign the different slopes to the reduction of every second NDI unit up to -1.06 V (C_{red} from

0 to 25%) and then reduction of every unit up to -1.24 V (C_{red} from 25 to 50%). In the interval between -1.24 and -1.29 V, the absorbance at 492 nm is constant, and the current approaches to zero (marked by a green shading and vertical green lines in Figure 2a,c). The data suggest that that P(NDI2OD-T2) is in its fully first reduced state (polaronic state, C_{red} = 50%).

Reduction set II: As a sharp reduction peak emerges with decreasing the potential further to -1.37 V (vertical purple line), the absorbance at 492 nm significantly drops, whereas the absorbance at 713 nm concomitantly rises. The sharp redox wave seems to correlate with the further uptake of electrons in P(NDI2OD-T2) to reach a doping level of C_{red} = 75%. After that, the current starts to decrease. At a more negative potential of -1.5 V (indicated by a vertical red line), the absorbance at 713 nm achieves its maximum for the formation of bipolarons and stays constant, while the absorbance at 492 nm falls to a constant low value (marked by a red shading in Figure 2a,c). Additionally, no current is detected from -1.6 to -1.84 V suggesting the fully bipolaron state at a doping level of C_{red} = 100%.

2.2. Absorption Behavior and Conductivity of Electrochemically-Doped Films

With the know-how on the potential-dependent existence of redox species, we applied potentiostatic doping to reach distinct doping levels in the P(NDI2OD-T2) films. More specifically, films were exposed to different electrochemical doping potentials and then further studied with respect to their absorption properties and conductivity behavior in the doped states after removing them from the electrolyte. We follow experimental procedures which we have developed for P3HT films.[51,66]

Figure 4a shows absorption spectra of P(NDI2OD-T2) films in the solid state doped at different electrochemical doping potentials. The neutral state has two characteristic bands at 395 and 701 nm which were obtained for the dry film before doping. The peak positions are very close to the blue spectrum in the in situ spectroelectrochemistry results at the beginning of the first CV cycle, see Figure S2c (Supporting Information). After reduction at -1.10 V, the absorption peak at 701 nm is smaller, while a new band appears at 493 nm, which we attribute to the formation of polaron species. At this doping level, the neutral state seems to be in coexistence with polaron species. The reduction at -1.30 V gives an absorption spectrum with characteristic peaks at 493, 708, and 801 nm, which closely resembles the fully polaron state in Figure S2c (Supporting Information). Please note that the UV–vis spectra of spin-coated films measured after solution doping with N-DMBI or vapor doping with TDAE show a small decrease in the absorption of the neutral band and a weak increase of the characteristic band at 489 and 800 nm for the radical anion formation.[37] The low doping efficiency with N-DMBI is attributed to the poor miscibility of dopant molecules with the polymer. In the case of TDAE, the dopant is highly volatile, and its reducing capability is too weak to access the significant reduction of the polymer (reduction potential of TDAE is -1.08 V vs Fc/Fc^+), leading to ineffective doping.[37] The electrochemical reduction at -1.67 V shows characteristic bands at 405 and 744 nm which are the signature of the bipolaron state. Overall, electrochemical doping outperforms chemical doping in terms of accessibility of the whole range of redox species in the solid state. The solid-state spectra clearly confirm that the redox species generated by electrochemical doping are stable in the solid state.

Going one step further we used four-line gold electrodes on glass substrates to electrochemically dope P(NDI2OD-T2) films and to subsequently measure solid-state conductivity of electrochemically doped films. The neutral state gives conductivities as low as $\sigma = 1.6 \pm 0.83 \times 10^{-6}$ S cm^{-1}, which is expected for non-doped conducting polymers. By decreasing the doping potential, the conductivity starts to rise until it develops a maximum at ≈-1.10 V versus Fc/Fc^+ with $\sigma = 2.6 \pm 1.1 \times 10^{-4}$ S cm^{-1}. The highest conductivity is found in a doped state when the neutral state is in coexistence with polaron species as indicated by the absorption spectra (Figure 4a,b). A further decrease of the doping potential to more negative values leads to a gradual decrease of the conductivity with a low conductivity at highest doping levels. Overall the conductivity behavior can be described as bell-shaped which resembles the behavior of redox polymers.[25] Therefore, it certainly differs from the plateau-like behavior found for P3HT in previous works.[51,52] As mentioned above P(NDI2OD-T2) can be considered a molecular redox system where the charge transport mechanism is described with the mixed-valence conductivity model.[67,68] Here, charge transport is governed by electron hopping between mixed redox sites. According to this model, for doped states where 100% polaron (C_{red} = 50%) or 100% bipolaron (C_{red} = 100%) are present in the film, the material should be less conducting than for the mixed valence states in between. Maximum conductivities are expected at half-doping levels, i.e., C_{red} = 25% and 75%. In the case of cyclic voltammetry coupled with in situ conductance measurements this behavior was confirmed by us in the literature.[24,37] The conductance profile in the forward and backward scans showed two maxima upon reduction, one at a potential of ≈-1.0 V versus Fc/Fc^+ in the range of the first reduction to polaron and the other ≈-1.40 V during the second reduction to the bipolaron.[37] It has to be noted that the conductance during the first reduction was much higher than the one for the second reduction, giving maximum conductance in the presence of the neutral state and polarons. Possible explanations for the low conductance in the presence of polarons and bipolarons (around C_{red} = 75%) include a large amount of counterions which has to be incorporated in the films for charge neutrality. This might hinder charge hopping between the redox sites, especially in the second reduced state.[37] In the in situ experiments also the effect of swelling needs to be considered.[69]

We have to note that although the electrochemical doping approach allows for a reproducible conductivity tuning over 3–4 orders of magnitude, the reported chemical doping approach with TDAE still gives higher maximum conductivities of 8×10^{-3} S cm^{-1}.[37] Reasons for this discrepancy are still under investigation and can probably be explained by different morphologies upon chemical and electrochemical doping.

One attempt to shed light onto this topic was done by the study of aligned films prepared by blade coating of highly concentrated solutions of P(NDI2OD-T2).[34] We showed before that pre-aggregated chains in solution can be aligned by applying shear forces, including the existence of liquid crystal-like phases. Further mechanistic studies were for example performed by Richter and coworkers.[70] The successful alignment of blade-coated films is evidenced by atomic force microscopy and

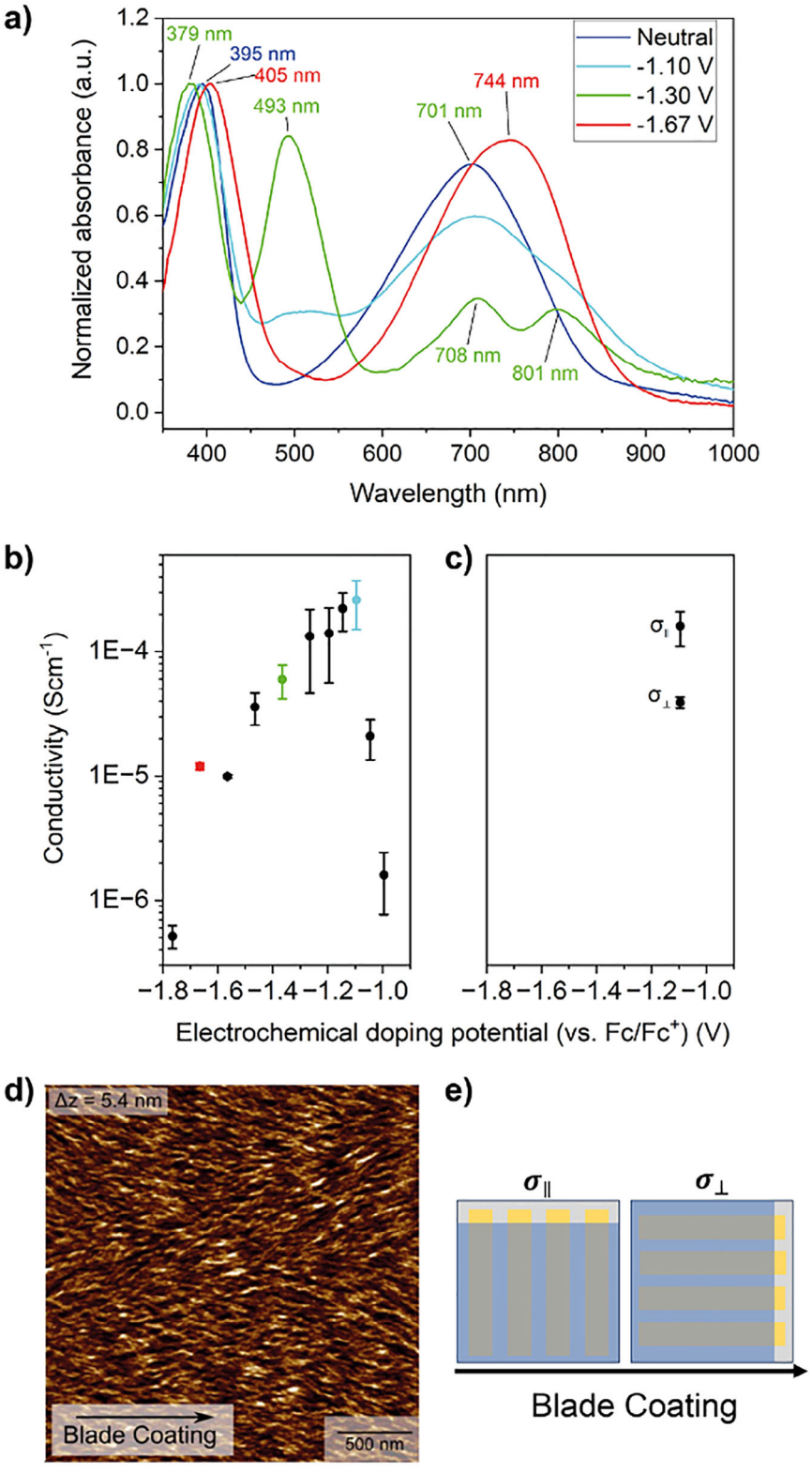

Figure 4. Optical and conductivity behavior of films in the solid state after electrochemical doping at specific doping potentials. a,b) The colored conductivity points in (b) correspond to the UV–vis-NIR spectra at the respective electrochemical doping potentials in (a), the films were spin-coated. c) Solid-state conductivity of blade-coated films of P(NDI2OD-T2) after electrochemical doping at -1.10 V (vs. Fc/Fc^+). The data show an anisotropic conductivity ratio of 4.1 along the chain versus perpendicular to the chain direction. d) AFM height image of a blade-coated film. e) Sketch showing film deposition by blade coating on top of 4-line electrodes to allow the measurements of anisotropic conductivity ratios.

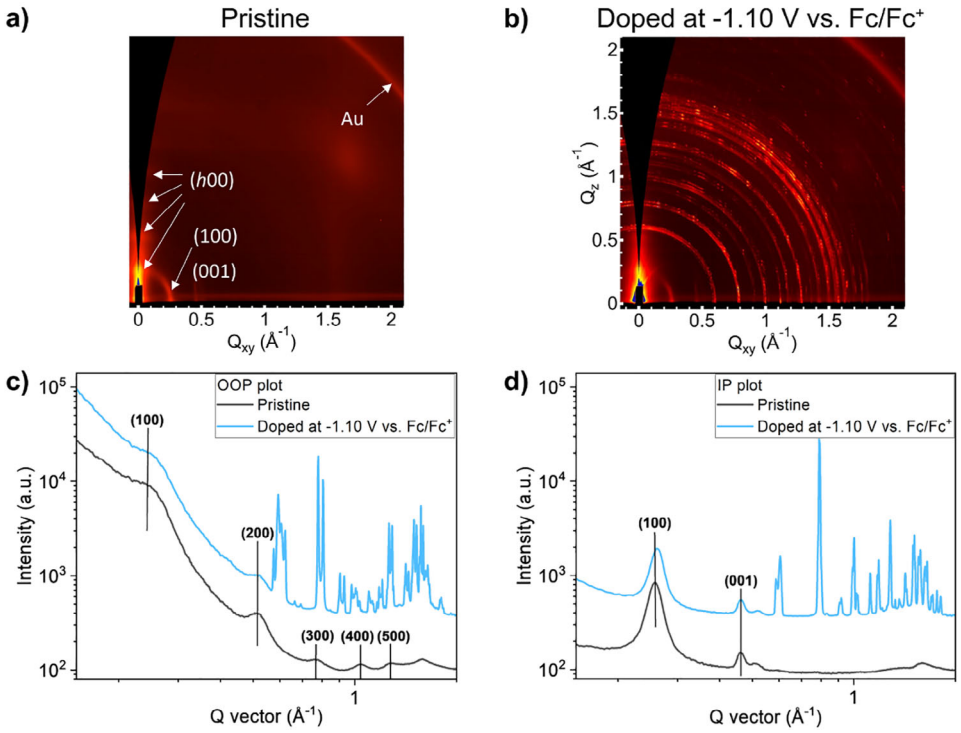

Figure 5. Ex situ measured GIWAXS data of aligned films of P(NDI2OD-T2) on gold substrates for the pristine neutral state a) and the reduced state doped at -1.10 V vs. Fc/Fc^+ in 0.1 M $TBAPF_6$/acetonitrile electrolyte b). The corresponding line cuts OOP and IP are presented in c,d). Samples are dried and transferred to the beamline under inert conditions.

GIWAXS pointing toward the alignment of fibers in the direction of blade coating (Figures 4d and 5). To probe the influence of the induced macroscopic alignment of the blade-coated films on the conductivity behavior, 4-line gold electrodes were coated both in parallel and perpendicular direction relative to the channels, Figure 4e. Since the measurement of conductivity suggests charge transport across the channels of the 4-line geometry, an alignment perpendicular to the channels results in a fiber orientation in the direction of the conductivity measurement. By coating parallel to the channels, the fibers become oriented perpendicular to the direction of the conductivity measurement.

Maximum conductivities with $\sigma_{\parallel} = 1.6 \pm 0.5 \cdot 10^{-4}$ S cm^{-1} could be measured in the direction of alignment, whereas measurements perpendicular to the alignment showed significantly lower values of $\sigma_{\perp} = 3.9 \pm 0.4 \cdot 10^{-5}$ S cm^{-1} (see Figure 4c). The maximum conductivity values differ by a factor of 4.1 comparing the directions parallel and perpendicular to the polymer fiber / chain direction. This shows the impressive influence of fiber alignment on the macroscopic conductivity also in the case of electrochemical doping. The reason why spin-coated films perform equally good as aligned films in measurement direction certainly offers room for interpretation. Spin coating distributes the material from the center of the substrate to the edges, producing films that typically show preferred alignment from the center of the substrate (radial).[71] Due to the geometry of our samples and the position of the channels, this radial alignment is more similar to the parallel alignment by blade coating and therefore might deliver values in the same order of magnitude. In general, the anisotropy of conductivity in the electrochemically doped and aligned films, indicates that the morphology is being preserved during doping and the concomitant ion insertion.

To understand the effect of doping on the microstructure of the film, grazing incidence wide-angle X-ray scattering (GIWAXS) of blade-coated samples was performed. The measurements were performed with the X-ray beam aligned parallel to the coating direction. GIWAXS measurements of the neutral film (neutral) shows distinct lamellar stacking peaks (h00) in both the IP and OOP directions along with an IP backbone (001) peak in **Figure** 5a, also indicated by black lines in the plots in Figure 5c,d. The pronounced (001) peak is consistent with the form I polymorph which is directly formed in as-cast films.[38]

The simultaneous presence of OOP and IP lamellar (100) peaks indicates a mixed orientation with both face-on and edge-on crystallites. It should be noted that a strong π–π stacking peak is absent which fits to findings in the literature.[41,72] With doping at -1.10 V (corresponding to the optimum conductivity) a large number of new peaks are seen which are most likely attributed to $TBAPF_6$ salt which remains at the film after electrochemical doping, Figure 5b. At this relatively low doping level the diffraction peaks of P(NDI2OD-T2) remain largely unaffected: all major peaks seen in the undoped film are seen in the low-doped film with only a subtle shift in the position of the IP (100) peak to high q (corresponding to a change in d-spacing from ≈24.5 to 24.0 Å). This change might be counterintuitive since an uptake of ions that requires a certain amount of space into the structure should lead to an increase in packing distance, however, similar behavior upon chemical doping has been reported before.[37] When doping to high levels (-1.50 V, Figure S8, Supporting

Information) the lamellar stacking d-spacing decreases further (to 23.3 Å) accompanied by a decrease in the relative intensity of the (001) backbone peak suggesting disruption of the molecular packing of P(NDI2OD-T2).

Near-edge X-ray absorption fine-structure (NEXAFS) spectroscopy was also performed to assess the surface structure (see Figure S9, Supporting Information). The neutral film exhibits a slightly edge-on surface orientation, consistent with P(NDI2OD-T2) exhibiting a distinct edge-on surface layer.[73] With low level doping, the spectrum and observed dichroism remain unchanged, suggesting that the top surface is still covered by P(NDI2OD-T2) with little change to molecular packing/molecular orientation (consistent with the GIWAXS results). With high-level doping, the spectrum changes significantly, indicating the presence of $TBAPF_6$ at the top surface.

3. Conclusion

The electrochemical reduction behavior of P(NDI2OD-T2) films was studied with in situ spectroelectrochemistry alongside with TD-DFT calculations allowing for the assignment of characteristic absorption spectra for different degrees of doping. The calculations showed very good agreement with the experimental spectra, in terms of characteristic features of the spectra, including the number and positions of the peaks. In particular, we can now explain why the absorption spectrum of neutral P(NDI2OD-T2) closely resembles that in the bipolaronic state. We also provide insights into why the absorption spectra of P(NDI2OD-T2) exhibit about twice as many peaks at corresponding doping levels compared to widely studied thiophene-based polymers.

Using potentiostatic doping P(NDI2OD-T2) films were charged at distinct doping levels in electrolyte and afterward removed from the electrolyte. Absorption spectroscopy was used to prove that the doped films could be transferred into the solid state. One highlight finding was that conductivities could be tuned over 3–4 orders of magnitude. Here, the highest conductivities are achieved at an intermediate doping level as it is predicted from the mixed valence conductivity model. Only the presence of mixed charged states allows for efficient charge transport in redox polymers like P(NDI2OD-T2). The strong tendency of this material to aggregate was beneficial to produce highly aligned films by blade coating. Films aligned in the direction of charge transport show similar conductivity values as spin-coated films being a factor of 4.1 higher than the conductivity of aligned films perpendicular to the direction of charge transport. Ex situ GIWAXS was performed to assess the influence of doping on the microstructure. For films doped at intermediate doping potentials which give rise to the highest conductivities, the doping causes little change to the crystalline packing of P(NDI2OD-T2). The measurements suggest that ion integration decreases the overall order as expected, but the initially induced texture is still preserved after the doping process.

We expect that the findings from this study do provide a deeper understanding of the interrelation between absorption behavior, charge transport, and film morphology in n-type conjugated redox polymers impacted by electrochemical doping. Especially in terms of increasing interest in water-based organic electrochemical transistors this know-how will be very beneficial for polymer and device preparation.

4. Experimental Section

Materials: The synthesis of P(NDI2OD-T2) was described in previous publications.[37,74] The molecular weight and PDI were $\overline{M_n}$ = 18 000 g mol^{-1}, PDI = 1.7, (HT-SEC). Solvents (chloroform and acetonitrile) and the electrolyte $TBAPF_6$ were purchased from Sigma-Aldrich. The indium tin oxide (ITO) covered glass substrates with a specified surface resistivity of ≤10 Ω sq^{-1} were purchased from Präzisions Glas & Optik Germany. For blade coating, P(NDI2OD-T2) with a molecular weight of $\overline{M_n}$ = 16 200 g mol^{-1} and a PDI of 2.8 was used.

Film Preparation: For spectroelectrochemistry and conductivity measurements, thin films of P(NDI2OD-T2) were prepared from solutions in chloroform at concentrations in the range of 3–5 g L^{-1}. The solutions were stirred for at least 1 h at 40 °C. Films were spin-coated on substrates which were cleaned by distilled water, isopropanol, and acetone in an ultrasonication bath beforehand. All films were prepared and stored in a glovebox under nitrogen atmosphere. For blade coating, solutions were prepared in chlorobenzene at a concentration of 20 g L^{-1} and stirred overnight at 80 °C. The distance between the blade and substrate was set to 100 µm. Blade coating was carried out on a Coatmaster 510 from Erichsen at a substrate temperature of 80 °C. Atomic force microscopy was performed on a Bruker Dimension Icon AFM in tapping mode.

In Situ Spectroelectrochemistry Measurements: Thin films of P(NDI2OD-T2) were prepared via spin coating from solutions in chloroform at a concentration of 5 g L^{-1} on ITO (indium tin oxide) covered glass substrates. The spin coating conditions were 2500 rpm for 60 s followed by 3000 rpm for 30 s. The spectroelectrochemical experiments were performed in the dark under argon atmosphere at room temperature. A UV–vis spectrometer from Zeiss was used in parallel with a Metrohm PGSTAT204 potentiostat for the cyclic voltammetry. The spectrometer was equipped with a CLH600 F halogen lamp, MCS611 2.2, and MCS621 vis II detectors. The CV measurements were conducted with a three-electrode setup. The setup consisted of the polymer film-covered ITO glass substrates which were used as the working electrode, a platinum wire as the counter electrode and a AgCl covered Ag wire as a pseudo-reference. CVs were recorded at a scan rate of 20 mV s^{-1} in 0.1 M $TBAPF_6$ in acetonitrile as electrolyte. The electrolyte was deaerated by argon bubbling before every measurement. After the measurement, a ferrocene/ferrocenium (Fc/Fc^+) redox couple was used as an internal standard to rescale the measured potentials. The half-wave potentials of P(NDI2OD-T2) were calculated using the equation

$$E_{1/2} = (Ep, red + Ep, ox)/2\ [eV] \quad (1)$$

with the reduction $E_{p.red}$ and oxidation peak potentials $E_{p.ox}$. By assuming that the redox potential of the Fc/Fc^+ redox couple is located at -4.8 eV in the Fermi scale, the LUMO level was obtained with equation[75]

$$E_{LUMO} = -(E_{onset} + 4.8)\ [eV] \quad (2)$$

DFT Calculations: All quantum chemical calculations in this study, including density functional theory (DFT) and time-dependent DFT (TDDFT) calculations, were performed using Gaussian16.[76] A dimer of NDI-T2 copolymer consisting of two naphthalene diimide (NDI) units with a methyl group attached to each phenyl ring and two bithiophene groups (T2) was used as the model system to simulate the electronic properties and optical absorption spectra of the neutral and negatively doped states. To save the computational cost, the octyl dodecyl sidechain was not considered and equipped the NDI unit with methyl groups, preserving the chemical structure of the π-conjugated backbone. An NDI-T2 dimer at its pristine/neutral states (Q = 0), and different negatively doped states (Q = -1 (C_{red} = 25%), Q = -2 (C_{red} = 50%), Q = -3 (C_{red} = 75%), and Q = -4 (C_{red} = 100%)) were first structurally optimized using DFT with both ωB97XD[2] and B3LYP hybrid functionals and 6–31+G(d) level of theory to obtain a

lowest energy structure at different reduction levels. The spin-restricted DFT calculations were performed for the charge-neutral/pristine state and the singlet state of the even number of charges (Q = -2 and Q = -4) and the spin-unrestricted calculation for the odd number of charges (Q = -1 and Q = -3) and the triplet states in optimizing the ground state in order to find the spin states having the lowest ground-state energy at all the charge levels as shown in Figure S6 (Supporting Information). The effect of the solvent (acetonitrile) was modeled implicitly by the polarizable continuum model (PCM), including the integral equation formalism variant (IEFPCM). The excited-state TDDFT calculations were performed on the optimized geometries of the neutral and reduced structures only for the spin-state having lowest ground-state energy, considering 40 excited states to obtain the UV-vis-NIR absorption spectra.

Conductivity Measurements: Custom-made 4-line gold electrodes were first evaporated on glass substrates. Thin films of P(NDI2OD-T2) were then spin-coated from solutions in chloroform at a concentration of 3 g L^{-1} on the gold electrodes with a channel width of 1 cm and a channel length of 100 µm. Spin coating conditions were 2000 rpm for 120 s followed by 6000 rpm for 15 s, resulting in film thickness of ≈30 nm.

The films were charged in a potentiostatic measurement in a three-electrode setup controlled by a Metrohm PGSTAT101 potentiostat. The electrolyte, the counter and reference electrodes were the same as described in the in situ spectroelectrochemistry measurements. After the electrochemical doping, charged films were removed from the setup. Conductivity measurements were conducted by a Keithley 2636 system source meter and operated using a self-written LabView program afterwards. The sample preparation and measurements were pursued under inert conditions.

GIWAXS Measurements: GIWAXS measurements were performed at the Australian Synchrotron utilizing the SAXS/WAXS beamline.[77] A Pilatus 2 M in-vacuum detector was used to acquire 2D scattering patterns with a silver behenate reference sample used to calibrate the sample-to-detector distance. The entire beam path was enclosed inside a vacuum flight tube to suppress background scatter. Images were taken as a function of the angle of incidence, with the angle that maximized scattering intensity (i.e., close to the critical angel) chosen. Data was analyzed using NIKA implanted in Igor Pro.[78]

NEXAFS Spectroscopy: NEXAFS measurements were performed at the Soft X-ray beamline at the Australian Synchrotron.[79] Measurements were performed under high vacuum, and X-ray absorption was measured using Total Electron Yield (TEY) mode where the drain current flowing to the sample to neutralize the photoelectrons emitted was recorded. Data was "double normalized" according to the stable monitor method and analyzed in QANT.[80] Further details can be found elsewhere.[81]

Supporting Information

Supporting Information is available from the Wiley Online Library or from the author.

Acknowledgements

X.S. and S.L. thank the Deutsche Forschungsgemeinschaft (DFG) for funding within the GRK2498. The work was performed in part at the SAXS/WAXS and Soft X-ray beamlines at the Australian Synchrotron, part of ANSTO. S.S.J. and S.G. thank the Department of Chemical Engineering, BITS Pilani, Pilani Campus. The calculations were performed on the SERB-funded HPC facility, grant number: SRG/2021/002169, and on resources provided by the Swedish National Infrastructure for Computing (SNIC) at NSC. I.Z. acknowledges the support from AFM@LIU, and the Swedish Research Council (project 2024–04449). The computations and data handling were enabled by resources provided by the National Academic Infrastructure for Supercomputing in Sweden (NAISS) at NSC@LiU partially funded by the Swedish Research Council through grant agreement no. 2022–06725.

Conflict of Interest

The authors declare no conflict of interest.

Author Contributions

D.N., X.S., and S.S.J. contributed equally to this work. D.N. performed experiments on the electrochemical doping, AFM and conductivity measurements. X.S. performed the in situ spectroelectrochemistry measurements. S.S.J., S.G., and I.Z. performed and analyzed the DFT calculations. W.T.L., L.T., and C.R.M. measured and analyzed GIWAXS and NEXAFS. S.L. made the concept and supervised the work. All authors contributed to and approved the manuscript.

Data Availability Statement

The data that support the findings of this study are available from the corresponding author upon reasonable request.

Keywords

anisotropic charge transport, conductivity spectroelectrochemistry, DFT calculations, electrochemical doping, n-type conducting polymers

Received: December 20, 2024
Revised: March 11, 2025
Published online: April 15, 2025

[1] I. E. Jacobs, A. J. Moulé, *Adv. Mater.* **2017**, *29*, 1703063.
[2] B. Lüssem, M. Riede, K. Leo, *Phys. Status Solidi A* **2013**, *210*, 9.
[3] K. A. Peterson, E. M. Thomas, M. L. Chabinyc, *Annu. Rev. Mater. Res.* **2020**, *50*, 551.
[4] L. Ding, Z.-D. Yu, X.-Y. Wang, Z.-F. Yao, Y. Lu, C.-Y. Yang, J.-Y. Wang, J. Pei, *Chem. Rev.* **2023**, *123*, 7421.
[5] J. Hynynen, D. Kiefer, L. Yu, R. Kroon, R. Munir, A. Amassian, M. Kemerink, C. Müller, *Macromolecules* **2017**, *50*, 8140.
[6] D. Kiefer, R. Kroon, A. I. Hofmann, H. Sun, X. Liu, A. Giovannitti, D. Stegerer, A. Cano, J. Hynynen, L. Yu, Y. Zhang, D. Nai, T. F. Harrelson, M. Sommer, A. J. Moulé, M. Kemerink, S. R. Marder, I. McCulloch, M. Fahlman, S. Fabiano, C. Müller, *Nat. Mater.* **2019**, *18*, 149.
[7] D. Yuan, E. Plunkett, P. H. Nguyen, D. Rawlings, M. L. Le, R. Kroon, C. Müller, R. A. Segalman, M. L. Chabinyc, *Adv. Funct. Mater.* **2023**, *33*, 2300934.
[8] D. Yuan, W. Liu, X. Zhu, *Chem. Soc. Rev.* **2023**, *52*, 3842.
[9] S. Wang, T.-P. Ruoko, G. Wang, S. Riera-Galindo, S. Hultmark, Y. Puttisong, F. Moro, H. Yan, W. M. Chen, M. Berggren, C. Müller, S. Fabiano, *ACS Appl. Mater. Interfaces* **2020**, *12*, 53003.
[10] C.-Y. Yang, M.-A. Stoeckel, T.-P. Ruoko, H.-Y. Wu, X. Liu, N. B. Kolhe, Z. Wu, Y. Puttisong, C. Musumeci, M. Massetti, H. Sun, K. Xu, D. Tu, W. M. Chen, H. Y. Woo, M. Fahlman, S. A. Jenekhe, M. Berggren, S. Fabiano, *Nat. Commun.* **2021**, *12*, 2354.
[11] H. Yan, Z. Chen, Y. Zheng, C. Newman, J. R. Quinn, F. Dötz, M. Kastler, A. Facchetti, *Nature* **2009**, *457*, 679.
[12] Y. M. Gross, S. Ludwigs, *Synth. Met.* **2019**, *253*, 73.
[13] J. Kim, X. Ren, Y. Zhang, D. Fazzi, S. Manikandan, J. W. Andreasen, X. Sun, S. Ursel, H. Un, S. Peralta, M. Xiao, J. Town, A. Marathianos, S. Roesner, T. Bui, S. Ludwigs, H. Sirringhaus, S. Wang, *Adv. Sci.* **2023**, *10*, 2303837.
[14] D. Jeong, I. Jo, S. Lee, J. H. Kim, Y. Kim, D. Kim, J. R. Reynolds, M. Yoon, B. J. Kim, *Adv. Funct. Mater.* **2022**, *32*, 2111950.

[15] I. P. Maria, S. Griggs, R. B. Rashid, B. D. Paulsen, J. Surgailis, K. Thorley, V. N. Le, G. T. Harrison, C. Combe, R. Hallani, A. Giovannitti, A. F. Paterson, S. Inal, J. Rivnay, I. McCulloch, *Chem. Mater.* **2022**, *34*, 8593.
[16] A. A. Szumska, I. P. Maria, L. Q. Flagg, A. Savva, J. Surgailis, B. D. Paulsen, D. Moia, X. Chen, S. Griggs, J. T. Mefford, R. B. Rashid, A. Marks, S. Inal, D. S. Ginger, A. Giovannitti, J. Nelson, *J. Am. Chem. Soc.* **2021**, *143*, 14795.
[17] J. Surgailis, L. Q. Flagg, L. J. Richter, V. Druet, S. Griggs, X. Wu, S. Moro, D. Ohayon, C. J. Kousseff, A. Marks, I. P. Maria, H. Chen, M. Moser, G. Costantini, I. McCulloch, S. Inal, *Adv. Mater.* **2024**, *36*, 2313121.
[18] M. Caironi, M. Bird, D. Fazzi, Z. Chen, R. Di Pietro, C. Newman, A. Facchetti, H. Sirringhaus, *Adv. Funct. Mater.* **2011**, *21*, 3371.
[19] V. D'Innocenzo, A. Luzio, A. Petrozza, D. Fazzi, M. Caironi, *Adv. Funct. Mater.* **2014**, *24*, 5584.
[20] S. Wang, H. Sun, U. Ail, M. Vagin, P. O. Å. Persson, J. W. Andreasen, W. Thiel, M. Berggren, X. Crispin, D. Fazzi, S. Fabiano, *Adv. Mater.* **2016**, *28*, 10764.
[21] Y. Liang, Z. Chen, Y. Jing, Y. Rong, A. Facchetti, Y. Yao, *J. Am. Chem. Soc.* **2015**, *137*, 4956.
[22] M. Arvind, C. E. Tait, M. Guerrini, J. Krumland, A. M. Valencia, C. Cocchi, A. E. Mansour, N. Koch, S. Barlow, S. R. Marder, J. Behrends, D. Neher, *J. Phys. Chem. B* **2020**, *124*, 7694.
[23] C. E. Tait, A. Reckwitz, M. Arvind, D. Neher, R. Bittl, J. Behrends, *Phys. Chem. Chem. Phys.* **2021**, *23*, 13827.
[24] D. Trefz, A. Ruff, R. Tkachov, M. Wieland, M. Goll, A. Kiriy, S. Ludwigs, *J. Phys. Chem. C* **2015**, *119*, 22760.
[25] C. Malacrida, Y. Lu, K. Dirnberger, S. Gámez-Valenzuela, M. C. Ruiz Delgado, S. Ludwigs, *J. Mater. Chem. C* **2020**, *8*, 15393.
[26] M. Brinkmann, E. Gonthier, S. Bogen, K. Tremel, S. Ludwigs, M. Hufnagel, M. Sommer, *ACS Nano* **2012**, *6*, 10319.
[27] M. Li, H. Bin, X. Jiao, M. M. Wienk, H. Yan, R. A. J. Janssen, *Angew. Chem., Int. Ed.* **2020**, *59*, 846.
[28] F. Panzer, H. Bässler, A. Köhler, *J. Phys. Chem. Lett.* **2017**, *8*, 114.
[29] Y. Zheng, Z. Yao, T. Lei, J. Dou, C. Yang, L. Zou, X. Meng, W. Ma, J. Wang, J. Pei, *Adv. Mater.* **2017**, *29*, 1701072.
[30] M. M. Nahid, A. Welford, E. Gann, L. Thomsen, K. P. Sharma, C. R. McNeill, *Adv. Electron. Mater.* **2018**, *4*, 1700559.
[31] R. Steyrleuthner, M. Schubert, I. Howard, B. Klaumünzer, K. Schilling, Z. Chen, P. Saalfrank, F. Laquai, A. Facchetti, D. Neher, *J. Am. Chem. Soc.* **2012**, *134*, 18303.
[32] R. Steyrleuthner, R. Di Pietro, B. A. Collins, F. Polzer, S. Himmelberger, M. Schubert, Z. Chen, S. Zhang, A. Salleo, H. Ade, A. Facchetti, D. Neher, *J. Am. Chem. Soc.* **2014**, *136*, 4245.
[33] W. L. Tan, L. Tang, R. Matsidik, G. Bryant, T. B. Martin, M. Sommer, D. M. Huang, C. R. McNeill, *Macromolecules* **2024**, *57*, 691.
[34] D. Trefz, Y. M. Gross, C. Dingler, R. Tkachov, A. Hamidi-Sakr, A. Kiriy, C. R. McNeill, M. Brinkmann, S. Ludwigs, *Macromolecules* **2019**, *52*, 43.
[35] L. Tang, L. Thomsen, C. R. McNeill, *ACS Appl. Polym. Mater.* **2022**, *4*, 5501.
[36] Y. Moon, Y. Kim, D. Yang, N. Han, M. Lee, Y. Kim, I.-Y. Jo, M.-H. Yoon, D.-Y. Kim, *J. Mater. Chem. A* **2024**, *12*, 5824.
[37] Y. M. Gross, D. Trefz, C. Dingler, D. Bauer, V. Vijayakumar, V. Untilova, L. Biniek, M. Brinkmann, S. Ludwigs, *Chem. Mater.* **2019**, *31*, 3542.
[38] C. Karunasena, J. R. Thurston, T. P. Chaney, H. Li, C. Risko, V. Coropceanu, M. F. Toney, J. Bredas, *Adv. Funct. Mater.* **2025**, 2422156.
[39] Y. Zhou, C. Fuentes-Hernandez, J. Shim, J. Meyer, A. J. Giordano, H. Li, P. Winget, T. Papadopoulos, H. Cheun, J. Kim, M. Fenoll, A. Dindar, W. Haske, E. Najafabadi, T. M. Khan, H. Sojoudi, S. Barlow, S. Graham, J.-L. Brédas, S. R. Marder, A. Kahn, B. Kippelen, *Science* **2012**, *336*, 327.
[40] R. A. Schlitz, F. G. Brunetti, A. M. Glaudell, P. L. Miller, M. A. Brady, C. J. Takacs, C. J. Hawker, M. L. Chabinyc, *Adv. Mater.* **2014**, *26*, 2825.
[41] Y. M. Gross, D. Trefz, R. Tkachov, V. Untilova, M. Brinkmann, G. L. Schulz, S. Ludwigs, *Macromolecules* **2017**, *50*, 5353.
[42] E. F. Aziz, A. Vollmer, S. Eisebitt, W. Eberhardt, P. Pingel, D. Neher, N. Koch, *Adv. Mater.* **2007**, *19*, 3257.
[43] P. Pingel, D. Neher, *Phys. Rev. B* **2013**, *87*, 115209.
[44] F. Borrmann, T. Tsuda, O. Guskova, N. Kiriy, C. Hoffmann, D. Neusser, S. Ludwigs, U. Lappan, F. Simon, M. Geisler, B. Debnath, Y. Krupskaya, M. Al-Hussein, A. Kiriy, *Adv. Sci.* **2022**, *9*, 2203530.
[45] Y. Song, J. Ding, X. Dai, C. Li, C. Di, D. Zhang, *ACS Mater. Lett.* **2022**, *4*, 521.
[46] O. Bardagot, Y. Kervella, A. A. Medjahed, S. Pouget, T. N. Domschke, A. Carella, C. Aumaître, P. Lévêque, R. Demadrille, *J. Mater. Chem. C* **2023**, *11*, 14108.
[47] Y. Yamashita, S. Jhulki, D. Bhardwaj, E. Longhi, S. Kumagai, S. Watanabe, S. Barlow, S. R. Marder, J. Takeya, *J. Mater. Chem. C* **2021**, *9*, 4105.
[48] S. Ghosh, N. Rolland, I. Zozoulenko, *Appl. Phys. Lett.* **2021**, *118*, 223302.
[49] D. Zhao, D. Kim, S. Ghosh, G. Wang, W. Huang, Z. Zhu, T. J. Marks, I. Zozoulenko, A. Facchetti, *Adv. Funct. Mater.* **2024**, *34*, 2310071.
[50] S. S. Jena, M. Garg, S. Ghosh, *Phys. Chem. Chem. Phys.* **2025**, *27*, 2177.
[51] D. Neusser, C. Malacrida, M. Kern, Y. M. Gross, J. Van Slageren, S. Ludwigs, *Chem. Mater.* **2020**, *32*, 6003.
[52] L.-S. Hornberger, D. Neusser, C. Malacrida, L. G. Kaake, S. Ludwigs, *Appl. Phys. Lett.* **2021**, *119*, 163301.
[53] K. Bruchlos, D. Trefz, A. Hamidi-Sakr, M. Brinkmann, J. Heinze, A. Ruff, S. Ludwigs, *Electrochim. Acta* **2018**, *269*, 299.
[54] J. Cornil, J. Brédas, *Adv. Mater.* **1995**, *7*, 295.
[55] G. Heimel, *ACS Cent. Sci.* **2016**, *2*, 309.
[56] U. Salzner, *J. Phys. Chem. A* **2008**, *112*, 5458.
[57] R.-Q. Png, M. C. Y. Ang, M.-H. Teo, K.-K. Choo, C. G. Tang, D. Belaineh, L.-L. Chua, P. K. H. Ho, *Nat. Commun.* **2016**, *7*, 11948.
[58] I. Zozoulenko, A. Singh, S. K. Singh, V. Gueskine, X. Crispin, M. Berggren, *ACS Appl. Polym. Mater.* **2019**, *1*, 83.
[59] I. Sahalianov, J. Hynynen, S. Barlow, S. R. Marder, C. Müller, I. Zozoulenko, *J. Phys. Chem. B* **2020**, *124*, 11280.
[60] R. Rubio-Govea, A. Opis-Basilio, A. Torres, M. Sánchez, K. Ray, K. A. Mazzio, *J. Phys. Chem. C* **2024**, *128*, 18612.
[61] S. Ghosh, V. Gueskine, M. Berggren, I. V. Zozoulenko, *J. Phys. Chem. C* **2019**, *123*, 15467.
[62] Y. Chen, S. Ghosh, X. Liu, I. V. Zozoulenko, M. Fahlman, S. Braun, *J. Phys. Chem. C* **2021**, *125*, 937.
[63] S. Ghosh, M. Berggren, I. Zozoulenko, *J. Phys. Chem. C* **2020**, *124*, 9203.
[64] A. Modelli, L. Mussoni, D. Fabbri, *J. Phys. Chem. A* **2006**, *110*, 6482.
[65] M. Wieland, C. Malacrida, Q. Yu, C. Schlewitz, L. Scapinello, A. Penoni, S. Ludwigs, *Flex. Print. Electron.* **2020**, *5*, 014016.
[66] D. Neußer, Electrochemical Doping of Semiconducting Polymer Films with Controlled Morphologies, Stuttgart, University of Stuttgart **2022**.
[67] D. Ofer, R. M. Crooks, M. S. Wrighton, *J. Am. Chem. Soc.* **1990**, *112*, 7869.
[68] A. Smie, J. Heinze, *Angew. Chem. Int. Ed. Engl.* **1997**, *36*, 363.
[69] R. Wu, M. Matta, B. D. Paulsen, J. Rivnay, *Chem. Rev.* **2022**, *122*, 4493.
[70] N. E. Persson, S. Engmann, L. J. Richter, D. M. DeLongchamp, *Chem. Mater.* **2019**, *31*, 4133.
[71] J. M. Chan, M. Wang, *Nano Lett.* **2022**, *22*, 5891.

[72] K. Tremel, F. S. U. Fischer, N. Kayunkid, R. D. Pietro, R. Tkachov, A. Kiriy, D. Neher, S. Ludwigs, M. Brinkmann, *Adv. Energy Mater.* **2014**, *4*, 1301659.
[73] T. Schuettfort, L. Thomsen, C. R. McNeill, *J. Am. Chem. Soc.* **2013**, *135*, 1092.
[74] V. Senkovskyy, R. Tkachov, H. Komber, M. Sommer, M. Heuken, B. Voit, W. T. S. Huck, V. Kataev, A. Petr, A. Kiriy, *J. Am. Chem. Soc.* **2011**, *133*, 19966.
[75] C. M. Cardona, W. Li, A. E. Kaifer, D. Stockdale, G. C. Bazan, *Adv. Mater.* **2011**, *23*, 2367.
[76] M. J. Frisch, G. W. Trucks, H. B. Schlegel, G. E. Scuseria, M. A. Robb, J. R. Cheeseman, G. Scalmani, V. Barone, G. A. Petersson, H. Nakatsuji, X. Li, M. Caricato, A. V. Marenich, J. Bloino, B. G. Janesko, R. Gomperts, B. Mennucci, H. P. Hratchian, J. V. Ortiz, A. F. Izmaylov, J. L. Sonnenberg, F. D. Williams, F. Lipparini, F. Egidi, J. Goings, B. Peng, A. Petrone, T. Henderson, D. Ranasinghe, V. G. Zakrzewski, et al., Gaussian 16 Rev. C.01, Wallingford, CT, **2016**.
[77] N. M. Kirby, S. T. Mudie, A. M. Hawley, D. J. Cookson, H. D. T. Mertens, N. Cowieson, V. Samardzic-Boban, *J. Appl. Crystallogr.* **2013**, *46*, 1670.
[78] J. Ilavsky, *J. Appl. Crystallogr.* **2012**, *45*, 324.
[79] B. C. C. Cowie, A. Tadich, L. Thomsen, *AIP Conf. Proc.* **2010**, *1234*, 307.
[80] E. Gann, C. R. McNeill, A. Tadich, B. C. C. Cowie, L. Thomsen, *J. Synchrotron Radiat.* **2016**, *23*, 374.
[81] M. M. Nahid, E. Gann, L. Thomsen, C. R. McNeill, *Eur. Polym. J.* **2016**, *81*, 532.

